buildings

MDPI

Article

Study on the Hysteretic Behavior of Post-Tensioned Unbonded Prestressed Concrete Beam–Column Joints with Two-Stage Energy Dissipation

Qiuyue Zhou [1], Xiaoyun Sun [1], Linjie Huang [2,3,*] and Yuxi Zhu [2,3]

[1] College of Civil Engineering, Nanjing Vocational Institute of Transport Technology, Nanjing 211188, China; qiuyuezhou@njitt.edu.cn (Q.Z.); xiaoyunsun@njitt.edu.cn (X.S.)
[2] College of Civil Engineering, Nanjing Forestry University, Nanjing 210037, China; zhuzhuxi@njfu.edu.cn
[3] Jiangsu Province Key Laboratory of Intelligent Construction and Safe Operation Maintenance of Bridges, Nanjing Forestry University, Nanjing 210037, China
* Correspondence: ljhuang@njfu.edu.cn

Abstract

To address the shortcomings of rapid stiffness degradation and single energy dissipation mechanisms in conventional post-tensioned unbonded prestressed concrete beam–column joints, this paper proposes a beam–column joint configuration that integrates a "friction-bending" two-stage energy dissipation mechanism. By adopting a low-prestress strategy, the joint enhances the energy dissipation ratio. Furthermore, energy dissipation bars with a secondary activation function in the energy dissipater form a stable third stiffness, thereby improving the hysteretic performance under large structural deformations. To clarify the influence of key design parameters on the hysteretic performance of the joint, this study established a refined finite element model using OpenSees3.3.0. A systematic parametric analysis was subsequently conducted, covering the number of prestressing tendons, initial prestress force, friction force, diameter of energy dissipation bars, and activation displacement ratio. The results indicate that the number of prestressing tendons only regulates the second stiffness and bearing capacity of the joint, with no significant effect on the energy dissipation capacity. The initial prestress force has limited influence on the joint stiffness and absolute energy dissipation; reducing the prestress can increase the equivalent viscous damping ratio by approximately 32%. The friction force is linearly and positively correlated with the activation force, enabling independent control of the joint's energy dissipation capacity. Increasing the friction force can enhance the energy dissipation per cycle by 21.7%, without affecting the stiffness at each stage. The third stiffness is dominated by the compression-bearing mechanism of the energy dissipation bars. Enhancing the third stiffness can increase the peak loading capacity of the joint by 28.7%, while slightly improving the ultimate energy dissipation capacity. The research finding can provide a theoretical basis for the collaborative optimization design that achieves "low prestress for efficiency enhancement, friction dissipation for guaranteed energy absorption, and third stiffness for safety assurance."

Keywords: post-tensioned; friction; hysteretic behavior; energy dissipation; self-centering; low prestress; parametric analysis

Check for updates

Academic Editor: Vipul Patel

Received: 22 August 2026
Revised: 15 September 2026
Accepted: 16 September 2026
Published: 19 September 2026

Copyright: © 2026 by the authors. Licensee MDPI, Basel, Switzerland. This article is an open access article distributed under the terms and conditions of the Creative Commons Attribution (CC BY) license.

1. Introduction

The traditional seismic design philosophy prioritizes life safety by allowing structures to dissipate energy through plastic deformation, which often results in high post-earthquake

repair costs and ultimately leads to irreparable damage and loss of functionality [1,2]. Consequently, research on low-damage or damage-free design and post-earthquake functional recoverability has become one of the key research directions in the field of earthquake engineering [3,4]. Post-tensioned unbonded prestressed concrete frames possess excellent deformation recovery capacity and favorable energy dissipation capability, making them one of the key structural systems for achieving recoverable functions. The post-earthquake functional recovery capacity of such structures is highly dependent on the proper configuration of high-performance energy dissipation devices. Sun et al. [5] proposed a new type of beam–column joint that combines angles and prestressing tendons to improve the hysteretic performance of the joint. Wu et al. [6] proposed a novel joint using prestressed tendons and bolts. The experimental results indicated that this joint dissipates significant seismic energy through pronounced deformation of the bolt angles, resulting in minimal residual displacement. Di et al. [7] proposed a novel energy dissipative beam–column joint using shape memory alloy (SMA) plates. By integrating SMA components with other energy dissipative elements, the self-centering and energy dissipation capabilities of joints can be effectively balanced, thereby enhancing the seismic performance of entire structures. Huang et al. [8] proposed a beam–column joint equipped with a replaceable multi-hole energy-dissipating joint device utilizing hinge holes and a hinge shaft, which significantly enhances the replaceability and replacement efficiency of the energy dissipater. Recent studies have advanced the theoretical and practical understanding of such joints. Hu et al. [9] derived key-point formulas for the moment–rotation hysteresis of a new post-tensioned unbonded connection, quantifying its energy dissipation coefficient; Zhong et al. [10] validated a decoupled parameter design in a hybrid joint with replaceable components (REC-PTH); and Yu et al. [11] reported an equivalent viscous damping of 13.4% in a precast self-centering RC beam–CFDST column joint through parametric analysis of tendon diameter and initial prestress.

Friction-based energy dissipation components achieve stable energy dissipation through the controlled slip between metal assemblies and friction plates under a set pretensioning force, and offer the advantage of post-earthquake non-replacement, thus becoming the most widely used energy dissipation form in this type of structure. Morgen and Kurama [12] were among the first to introduce an energy dissipation mechanism into post-tensioned unbonded concrete beam–column joints. Subsequently, Cheng et al. [13] and Huang et al. [14] proposed joint configurations with web friction and top-bottom friction energy dissipation, respectively, which significantly reduced member damage under moderate to strong earthquakes. To further address the issue of degradation in self-centering capacity caused by relaxation, creep, and other factors of prestressing tendons, Lu et al. [15] developed a self-centering friction energy dissipater that integrates both energy dissipation and self-centering mechanisms, and successfully applied it to joint design. Qiu et al. [16] proposed a joint system combining friction energy dissipation with SMA (Shape Memory Alloy), which achieved excellent synergistic performance in self-centering and energy dissipation without relying on prestressing tendons. At the theoretical research level, Koshikawa et al. [17] thoroughly revealed the mechanical behavior of post-tensioned unbonded joints with friction devices and established design formulas covering key indicators such as flexural capacity and energy dissipation coefficient. Furthermore, based on vulnerability analyses under the action of major and extremely large earthquakes, Kammula et al. [18] and Wu et al. [19] systematically verified the significant advantages of self-centering concrete frames over conventional frames in terms of collapse resistance and functional recoverability. Zhao et al. [20] tested a precast self-centering energy-dissipative joint (PSC-ED) that combines self-centering rebar couplers with replaceable unidirectional friction dampers, thereby validating the post-earthquake rapid-recovery

concept. Li et al. [21] conducted a parametric study on self-centering precast frame connections with composite damping, identifying threshold effects of friction-plate and end-plate thickness on friction–plastic synergy. Recent studies have further advanced the state of the art in self-centering prestressed connections. Wang et al. [22] demonstrated that combining low prestress with sloped friction dissipators in precast frames substantially reduces beam and column internal forces under major earthquake shaking and lowers repair costs, confirming the engineering value of the low-prestress strategy beyond single-joint tests. Chaisanit et al. [23] integrated unbonded post-tensioned tendons with buckling-restrained knee braces in precast joints and reported a 47% gain in relative self-centering efficiency, showing that external hysteretic devices can be decoupled from the PT re-centering system. Wang et al. [24] proposed a post-tensioned precast hybrid connection with replaceable energy-dissipating elements and showed that replacing the dissipaters alone restores seismic capacity after damage, which aligns with the replaceable-design direction of the present joint. Yılmaz and Oğuz [25] numerically confirmed that embedding frictional–elastomeric devices into RC beams stabilizes hysteretic loops at large drift when multiple longitudinal plates are used, supporting the friction-stage design in this study. On the durability side, Guo et al. [26] investigated the long-term behavior of web-friction self-centering frames and quantified prestress loss and bolt relaxation effects, supporting the durability discussion in our future-work outlook.

Conventional unbonded post tensioned self-centering joints originating from the PRESSS program exhibit a flag shaped hysteresis with limited energy dissipation and a sharp post opening stiffness drop [12,17,27,28]. To mitigate this, supplementary dissipaters such as ribbed angles [5], shape memory alloy plates [7], shape memory alloy friction devices [16], sloped friction energy [29] were introduced, yet the single activation nature remained. Recently, the low-prestress (LP) system proposed by Xiao et al. [30] and Zheng et al. [31] effectively alleviates the structure's reliance to enhance relative energy dissipation ratio. Huang et al. [32] and Hu et al. [9] addressed friction bending composite behavior and third stiffness emergence in post tensioned joints. Zhong et al. [10], Zhao et al. [20], and Wang et al. [24] explored replaceable dissipaters. Yu et al. [11] reported an equivalent viscous damping ratio of approximately 13.4% in a precast self-centering reinforced concrete beam to concrete filled double skin steel tubular column joint. Chaisanit et al. [23] and Wang et al. [22] confirmed the low prestress strategy at frame level. Yılmaz and Oğuz [25] stabilized hysteretic loops with frictional elastomeric devices. However, except for Huang et al. [32], who were limited to three experimental variables, none of these studies systematically decoupled five parameters in a concrete joint, nor quantified the low prestress damping gain within a multi parameter framework. Long-term studies by Guo et al. [26] and Cheng et al. [13] quantified prestress and bolt relaxation but did not link degradation to two stage parameter design. This study fills that gap by implementing secondary energy dissipation bar activation in a post-tensioned unbonded prestressed joint, parametrizing number of prestressing tendons, initial prestress force, friction force, diameter of energy dissipation (ED) bars, and activation displacement ratio over eleven cases, and establishing the three stage stiffness decoupling law with an approximately 32% equivalent viscous damping ratio gain under low prestress and a 28.7% peak capacity gain from the third stiffness. The research methodology flowchart of this study is shown in Figure 1.

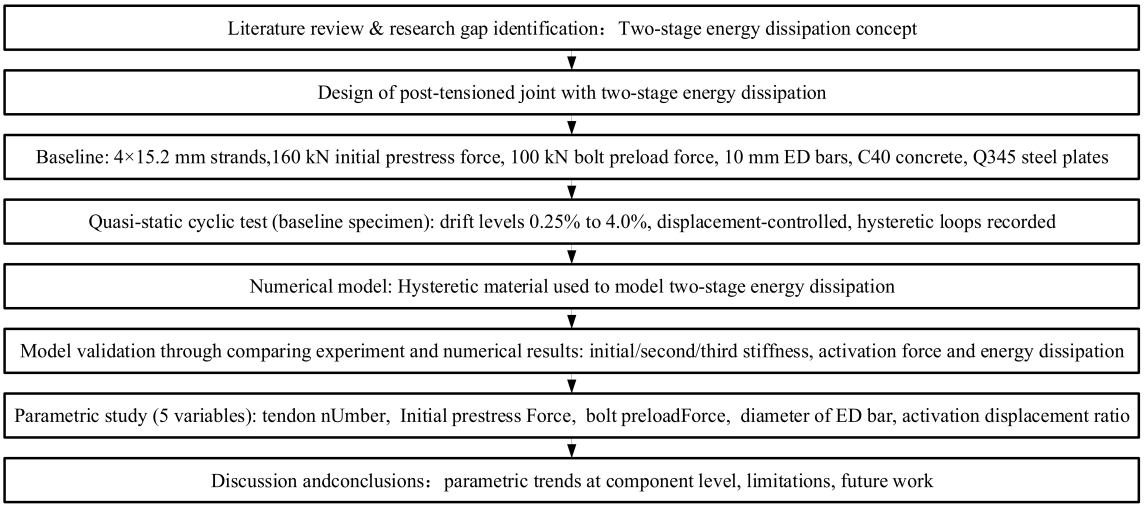


Figure 1. Research methodology flowchart.

2. Configuration and Theoretical Hysteretic Behavior of Post-Tensioned Unbonded Prestressed Concrete Beam–Column Joints with Two-Stage Energy Dissipation

The configuration of the post-tensioned unbonded prestressed concrete beam–column joints with two-stage energy dissipation is illustrated in Figure 2. As depicted in Figure 2, the energy dissipater in this joint primarily consists of two components. The first component provides friction energy dissipation and comprises specific parts such as pretensioned high-strength bolts, external plates, inner plates, and friction pads. The second component consists of energy dissipation bars (ED bars) that achieve bending energy dissipation. In this setup, the external plates are connected to the column end, while the outer surface of the inner plates is embedded with friction pads and cast integrally with the beam end. The shear resistance at the beam–column interface is collectively provided by the contact pressure between the friction pads, the high-strength bolts, and corbels.

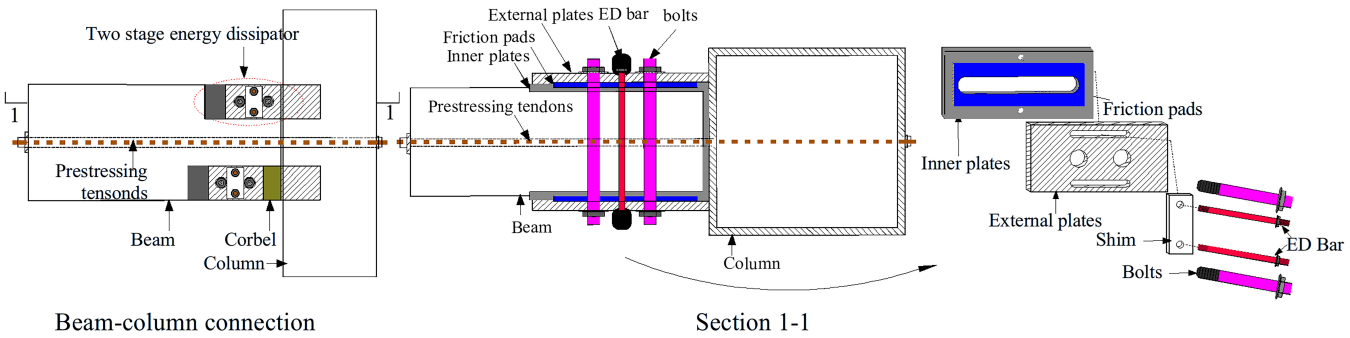


Figure 2. Configuration of post-tensioned unbonded prestressed concrete beam–column joints with two-stage energy dissipation.

At the initial loading stage, the beam–column joint opens, and relative slip occurs between the inner and external plates, triggering the friction energy dissipation mechanism. As the joint opening displacement increases, the ED bars come into contact with and bear against the elongated hole walls of the external plates, causing the energy dissipater to transition into the "friction-bending" composite energy dissipation stage.

Compared with the conventional flag-shaped hysteretic behavior, this joint achieves a larger energy dissipation ratio β (i.e., the ratio of the energy dissipation system's contribution to that of the self-centering system) through a low-prestress strategy. Leveraging the

secondary activation mechanism of the energy dissipater, a stable third stiffness K_3 and enhanced energy dissipation capacity are developed during the large deformation stage. These dual strengthening mechanisms significantly improve the energy dissipation capacity and lateral stiffness of the structure under strong earthquakes (or large deformations), effectively suppressing dynamic responses and deformation concentration effects, thereby reducing the overall seismic losses of the structure.

Figure 3a illustrates the load–displacement relationship of the joint under ideal loading conditions, where Δ denotes the beam-end displacement and F is the joint load. Figure 3b depicts the three-stage moment–relative rotation (M–θr) curve of the joint under cyclic loading, with θ_r representing the relative rotation at the beam–column interface. The overall mechanical response is characterized by six distinct phases:

(1) 0–1: Joint decompression phase. Before loading, the bolts of the energy dissipater apply a pretensioning force to press the internal components together and generate friction. The precast beam and column are connected into a monolithic unit by low-prestress tendons, resulting in a high compressive stress at the beam–column contact interface. Studies have shown that the joint stiffness in this phase can be considered equivalent to that of a traditional cast-in-place reinforced concrete joint [33].

(2) 1–2: Critical opening phase. As the beam-end load increases, the rotation of the beam is restrained by the friction device. When the load increases to Point 2, the friction force reaches its maximum value, and the beam–column contact interface is at a critical state just before opening. The corresponding load is F_1, and the moment is the critical opening moment M_{IGO}.

(3) 2–3: Joint pure friction sliding phase. When the external load increases to the sum of the initial prestress of the prestressing tendons and the friction force (corresponding to the unloading force F_1 at Point 2), a gap appears at the joint and widens with increasing load. The beam and column members develop a relative rotation θ about the center of rotation. The friction energy dissipater enters the sliding friction stage, and the friction force remains constant. During joint opening, the prestressing tendons elongate, leading to a corresponding increase in the moment they resist.

(4) 3–4: Contact of energy dissipation bars with hole walls and secondary activation of the energy dissipater. When the load increases to Point 3, the energy dissipation bars come into contact with and are compressed by the elongated hole walls of the external plate, marking the secondary activation of the energy dissipater. The compressed energy dissipation bars generate a third stiffness k_3, providing additional flexural stiffness to the joint. At this point, the energy dissipation mechanism transitions from a single friction mode to a composite mode combining friction slip and bar bending, with a significant enhancement in energy dissipation capacity. The joint stiffness is primarily provided by the energy dissipation bars and the prestressing tendons, showing a marked increase compared to the previous phases.

(5) 4–6: Joint reverse sliding phase. Unloading begins when the prestressing tendons have not yet yielded (Point 4). The beam-end load decreases, and the friction force drops from its maximum positive value to zero and then increases in the reverse direction to its maximum value (Point 5). During this phase, the joint rotation remains unchanged, the moment decreases by $2M_f$, and the gap opening reduces. From Stage 5 to 6, the gap gradually closes. The energy dissipation bars return to their initial positions through plastic deformation, and the energy dissipation mechanism shifts from the composite mode back to the single friction mode. Because the friction force is much smaller than the prestress of the tendons, the joint stiffness in this phase mainly depends on the prestressing tendons, similar to Phase 2–3. At Point 6, the

energy dissipater resets, and the rotational point at the top of the beam re-contacts the column.

(6) 6–7: Joint closing phase. The prestress force causes the compressive stress at the contact interface between the beam flange and the column to gradually increase. At Point 7, the joint basically returns to its initial state, with minimal and controllable residual deformation, and the overall residual displacement meets the requirements. At this point, the joint is about to withstand reverse loading. The rotational point shifts from the lower beam flange to the end of the upper beam flange, and the mechanical behavior of each component during the reverse loading phase is completely consistent with that of the forward loading phase.

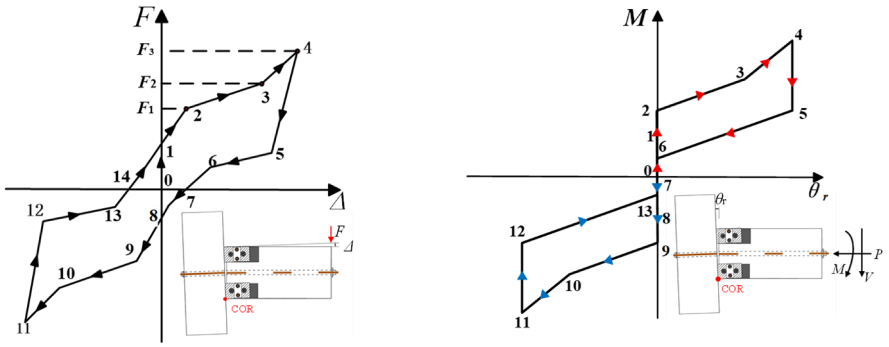


Figure 3. Hysteretic curve of post-tensioned unbonded prestressed concrete beam–column joints with two-stage energy dissipation. (**a**) Load–displacement relationship curve; (**b**) Moment–rotation relationship curve.

From above analyses, it can be seen that the difference between this joint and existing post-tensioned unbonded prestressed structures lies in its distinct third stiffness K_3. The third stiffness K_3 is contributed by the combined flexural stiffness of the ED bars, the axial stiffness of the prestressed tendons, and the beam–column components. The expression has been derived by Huang et al. and is shown in Equation (1). This relationship has been validated against the original experimental backbone by Huang [32], with a discrepancy of less than 15%.

$$k_3 = \frac{9.6E_cI_bI_cL_b^2mk_s(d')^2\Delta_b(mk_s + k_b - mk_b)}{\left[9.6E_cI_bI_c\Delta_1h_b - \left(n\mu F_{pc}\sum_{i=1}^{2} d_{fi} + F_{T0}d' - F_1d'\right)L_b^3\right](mk_s + k_b)l_{ob}} + \frac{3\pi Ed^4}{L_{bt}} \quad (1)$$

where E_c is the elastic modulus of the concrete, I_b and I_c are the sectional moments of inertia of the beam and the column respectively, L_b is the length of the beam, m is the number of prestressed tendons, k_s and k_b denote the axial stiffness of the steel strand and the frame beam respectively, Δ_b is the displacement of the energy dissipating bar, Δ_1 is the opening displacement of the joint, h_b is the height of the beam section, n is the number of friction interface, μ is the friction coefficient, F_{pc} is the total bolt pretension force, F_{T0} is the initial prestress force, d' is the distance from the beam axis to the rotation point, F_1 is the opening force of the joint, and l_{ob} is the distance between the energy dissipating bar and the rotation point.

3. Beam–Column Joint Specimen and Finite Element Model

3.1. Beam–Column Joint Information

The analytical model adopts the joint specimen tested by Huang et al. [32]. The dimensions of the beam and column, reinforcement details, and energy dissipater dimensions

are shown in Figures 4a and 4b, respectively. Both the precast column and the precast beam were made of C40 concrete (where C40 denotes a concrete compressive strength of 40 MPa), with a length of 1800 mm for each. The column and beam cross-sections were 400 × 400 mm and 250 × 450 mm, respectively. Four 1 × 7-strand steel strands with a nominal diameter of 15.2 mm were selected as the prestressing tendons, with an initial prestress force of 160 kN and total bolt pretensioning force of the energy dissipater set to 100 kN. All reinforcing bars were HRB400 steel with a yield strength of 400 MPa, while the stirrups were HPB300 steel with a yield strength of 300 MPa. The longitudinal reinforcement of the column consisted of 12 bars with a diameter of 22 mm, and the stirrups were 8 mm diameter bars spaced at 100 mm. The longitudinal reinforcement of the beam consisted of 4 bars with a diameter of 12 mm and 8 bars with a diameter of 22 mm, and the stirrups were 8 mm diameter bars spaced at 100 mm.

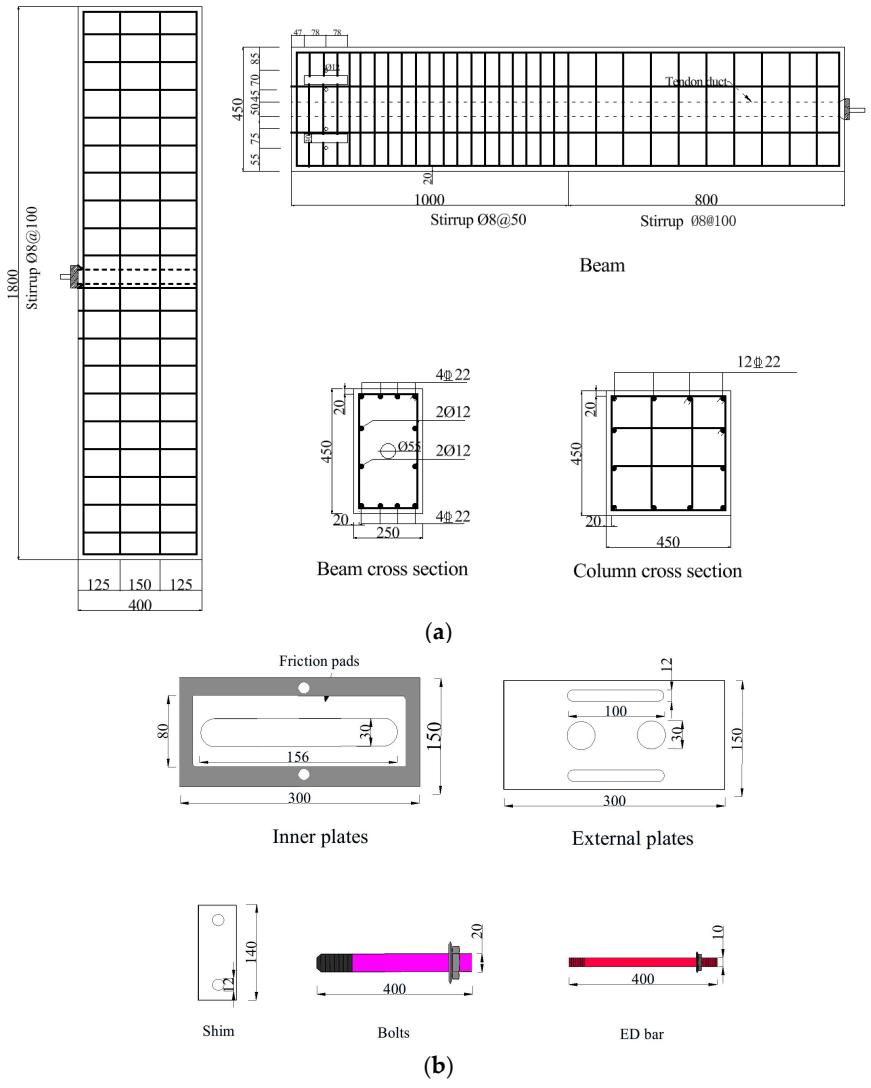


Figure 4. Dimensionof beam–column joint and energy dissipator. (**a**) Dimension and reinforcement of beam and column. (**b**) Dimension of energy dissipator.

A 50 mm diameter hole was reserved in both the beam and the column to accommodate four 15.2 mm diameter unbonded prestressing tendons. The friction coefficient between the contact surface of the friction pads and the external plates is 0.3. Meanwhile, holes were also reserved in the beam for the bolts and energy dissipation bars to pass through, facilitating the joint of the energy dissipater. The external plates were provided with standard 20 mm

diameter round holes for the 18 mm diameter high-strength bolts, and elongated holes (slotted holes) with a diameter of 30 mm and a length of 156 mm for the 10 mm diameter energy dissipation bars. This design avoids collision between the friction bolts and the hole edges during construction, ensures a large relative rotation between the beam and column, and guarantees that the energy dissipation bars are subjected to compression and bending to achieve the secondary activation of the energy dissipater.

To simulate the opening and closing behavior of the frame joint under horizontal loading, a vertical cyclic load was applied at the beam end during the test. During the loading process, the displacement amplitudes corresponded successively to the joint displacements at drift ratios of 0.5%, 1.0%, 1.5%, 2.0%, 2.5%, 3.0%, 3.5%, and 4.0%.

3.2. Numerical Model of Beam–Column Joint

The joint configuration is a key factor influencing the mechanical behavior of post-tensioned unbonded prestressed concrete frames. A numerical analysis model of post-tensioned unbonded prestressed concrete beam–column joints with two-stage energy dissipation was developed using the finite element software OpenSees3.3.0, as shown in Figure 5. The hysteretic behavior of the joint can be decomposed into the combination of a prestressed beam–column joint (Figure 5a) and a beam–column joint with an energy dissipator (Figure 5b). Nonlinear beam–column elements were used to simulate the precast concrete beam and column members, in which the Concrete01 material model, neglecting the tensile strength of concrete, was adopted for the concrete. The peak compressive strain is 0.002 and the ultimate compressive strain is 0.0038; tensile strength is neglected (the envelope drops to zero at zero strain).

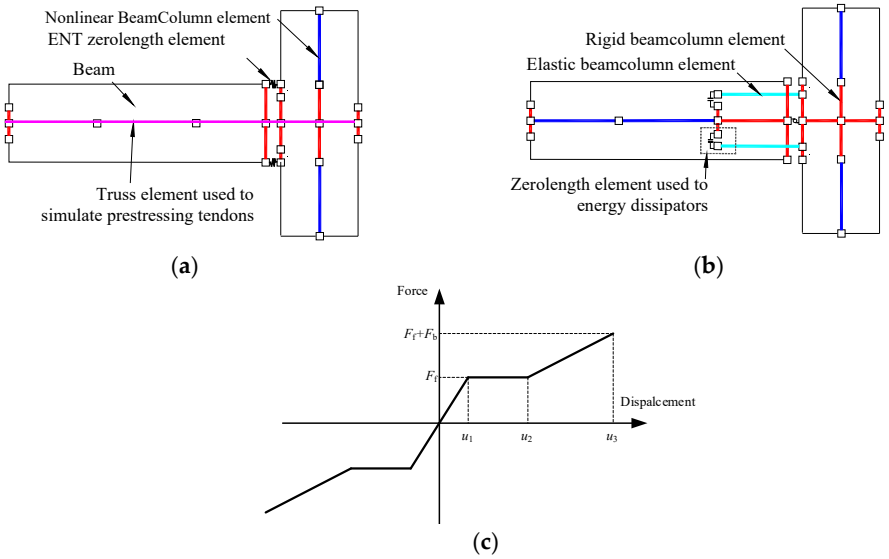


Figure 5. Numerical model of beam–column joints. (**a**) Prestressed beam–column joint. (**b**) Beam–column joint with an energy dissipator. (**c**) Force–displacement backbone of hysteretic material.

The prestressing tendons were modeled using truss elements assigned to a Steel02 constitutive model with an initial strain. This material formulation captures the Bauschinger effect and isotropic hardening under cyclic loading, with transition parameters set to R_0 = 20, cR = 0.925, a_1 = 0.925.

The prestress was initialized through its initial strain parameter to apply the specified initial stress. In the simulation of post-tensioned unbonded prestressed beam–column joints, the key to allowing the prestressing tendons to be stretched with joint deformation lies in simulating the characteristic that the contact rotational points of the beam and column can only resist compression but not tension. To simulate this feature, zero-length

elements (ZeroLength) with the UniaxialMaterial ENT (Elastic No-Tension) material, which allows only compression and no tension, were adopted at the two rotational points at the top and bottom of the joint to simulate the opening and closing behavior of the joint, shown in Figure 5a.

The steel plate assemblies in the energy dissipater were simulated using ElasticBeam-Column based on the Steel02 constitutive model, with one end connected to the column and the other end connected to the equivalent action point of the bolt pretensioning force in the energy dissipater on the beam. Meanwhile, ZeroLengthSection elements were used to simulate the friction unit, and a Hysteretic material was assigned to it to simulate the aforementioned two-stage friction–bending composite energy dissipation behavior, shown in Figure 5c.

The force–displacement backbone of the prescribed Hysteretic material, illustrated in Figure 5c, encompasses elastic deformation, frictional slip, slotted-hole contact, bar bending, and bearing. The positive and negative envelope points ($\pm u_1$, $\pm F_f$), ($\pm u_2$, $\pm F_f$), ($\pm u_3$, $\pm(F_b+F_f)$) correspond to those identified in Figure 5c. The pinching parameters (pinchx = 0.8, pinchy = 0) and damage parameters (damage1 = 0.01, damage2 = 0.01, beta = 0.04) are physically justified by the elastic-gap mechanism. Here, F_f and F_b represent the friction resistance provided by the contact surfaces and the bearing capacity contributed by the bending of the energy-dissipating bars, respectively, with their expressions given in Equations (2) and (3).

$$F_f = n\mu F_{pc} \tag{2}$$

where n is the number of friction interface, μ is the friction coefficient, F_{pc} is the total bolt pretensioning force.

$$F_b = \frac{3(u_3 - u_2)E\pi d^4}{L_{bt}^3} \tag{3}$$

where u_1 denotes the elastic deformation of the dissipater, which can be determined from the material properties of the steel plates; u_2 is the gap between the dissipative bar and the reserved circular hole in the beam, i.e., the length of the pure planar sliding stage; u_3 is the displacement of the ED bar after it contacts the edge of the hole. E is the modulus of elasticity of the ED bar material, d is the diameter of the ED bar, and L_{bt} is the total length of the ED bar.

Once the backbone curve of the Hysteretic material shown in Figure 5c is defined, the activation force of the dissipater can be directly obtained. Furthermore, the relationship between the ED bar diameter and the assigned numerical response can be derived from Equations (1) and (3).

The numerical simulation method adopted in this study was verified using the low-cycle reversed loading test results of the two-stage energy dissipation post-tensioned unbonded prestressed concrete beam–column joint reported by Huang et al. [32]. Figure 6 compares the simulated joint moment–drift curves with the experimental results. The results show a high degree of consistency between the simulated and experimental curves in terms of overall shape, stiffness degradation trend, and pinching effect. In addition, as shown in Table 1, a quantitative comparison between the experimental and numerical results was conducted at the maximum drift amplitude (4%) to comprehensively evaluate the accuracy of the numerical model. Considering the symmetry of the hysteretic curves, the values for each metric in Table 1 are averaged from both positive and negative loading cycles, covering key indicators including initial stiffness (k_1), second stiffness (k_2), third stiffness (k_3), positive and negative peak moment, equivalent viscous damping ratio, residual drift. The comparison shows that the errors for initial and second stiffness are 7.5% and 5.6%, respectively, indicating good agreement, while the deviation for third stiffness is −14.1%, which is within an acceptable range. This demonstrates that the established

computational model can reasonably reproduce the nonlinear mechanical behavior of the specimen during cyclic loading, providing a reliable numerical basis for subsequent structural performance evaluation. It should be noted that the above validation is based on a single quasi-static cyclic test and represents component-level verification; the generalizability of the findings requires further confirmation through multi-specimen statistical analysis in future work. The concrete in the numerical model was represented by a C40-equivalent constitutive relation with strength and elastic stiffness calibrated from conventional mix designs. The reasonableness of using ordinary Portland cement concrete strength and stiffness assumptions is further supported by independent studies on sustainable concrete mixes, which report comparable workability and strength characteristics for metakaolin-modified laterite aggregate concrete [34] and for concrete incorporating waste glass cullet and snail shell powder [35].

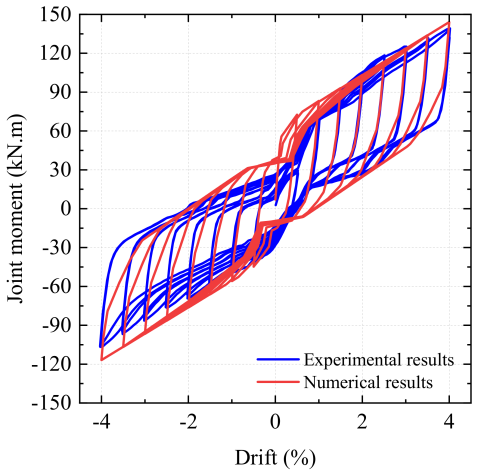


Figure 6. Comparison between experimental and numerical results.

Table 1. Comparison metrics of experimental and numerical results.

Comparison Metrics	Experimental Results	Numerical Results	Error
K_1 (kN/mm)	3.45	3.73	7.5%
K_2 (kN/mm)	0.67	0.71	5.6%
K_3 (kN/mm)	0.89	0.78	−14.1%
Equivalent viscous damping ratio at 4% drift (%)	13.5	15.2	11.2%
Maximum moment (kN.mm)	123.5	129.4	4.6%
Residual drift at 4% drift (%)	1.1	1.3	15.3%

4. Parametric Analysis of the Hysteretic Performance of Beam–Column Joint

4.1. Analysis Cases

To further evaluate the influence of energy dissipater parameters and prestressing tendon parameters on the hysteretic performance of the joint, a series of beam–column joint models were developed based on the aforementioned joint specimen. The configuration parameters, including the number of prestressing tendons, initial prestress force, bolt pretensioning force, diameter of energy dissipation bars, and the activation displacement ratio of the energy dissipater (pure friction segment length/total deformation of the energy dissipater), were sequentially adjusted to conduct a parametric analysis. The specific parameters are listed in Table 2. The parameter ranges adopted in this study, including 3 to 5 tendons, initial prestress of 80 to 300 kN, bolt preload of 50 to 135 kN, ED bar diameter

of 10 to 14 mm, and activation ratio of 0.25 to 0.50, all fall within the design limits of the original experiment reported by Huang et al. [32]. None of these values exceed the allowable stress or strain capacities of the constituent materials.

Table 2. Parametric finite element analysis model of beam–column joint.

Case	Number of Prestressing Tendons	Initial Prestress Force/kN	Bolt Pretensioning Force/kN	Diameter of Energy Dissipation Bars/mm	Activation Displacement Ratio
Case 1	4	160	100	10	0.25
Case 2	3	160	100	10	0.25
Case 3	5	160	100	10	0.25
Case 4	4	80	100	10	0.25
Case 5	4	300	100	10	0.25
Case 6	4	160	50	10	0.25
Case 7	4	160	135	10	0.25
Case 8	4	160	100	12	0.25
Case 9	4	160	100	14	0.25
Case 10	4	160	100	10	0.38
Case 11	4	160	100	10	0.50

In Case 1, Case 2, and Case 3, the number of prestressing tendons were designed as 4, 3, and 5, respectively, while the initial prestress force, bolt pretensioning force, diameter of energy dissipation bars, and activation displacement ratio of the energy dissipater were kept identical. The influence of the number of prestressing tendons on the hysteretic performance of the joint was studied through comparative analysis.

In Case 1, Case 4, and Case 5, the initial prestress forces were designed as 160 kN, 80 kN, and 300 kN, respectively, while the number of prestressing tendons, bolt pretensioning force, energy dissipation bar diameter, and activation displacement ratio of the energy dissipater were the same. The influence of initial prestress force on the hysteretic performance was investigated through comparative analysis.

In Case 1, Case 6, and Case 7, the bolt pretensioning forces were set to 100 kN, 50 kN, and 135 kN, respectively, while the number of prestressing tendons, initial prestress force, energy dissipation bar diameter, and activation displacement ratio of the energy dissipater were identical. The influence of bolt pretensioning force on the hysteretic performance was examined through comparative analysis.

In Case 1, Case 8, and Case 9, the third stiffness values were designed as 2.7 kN/mm, 3.2 kN/mm, and 3.6 kN/mm, respectively, while the number of prestressing tendons, bolt pretensioning force, initial prestress force, and activation displacement ratio of the energy dissipater were the same. The influence of the energy dissipation bars on the hysteretic performance was studied through comparative analysis.

In Case 1, Case 10, and Case 11, the activation displacement ratios of the energy dissipater were designed as 0.25, 0.38, and 0.50, respectively, while the number of prestressing tendons, bolt pretensioning force, initial prestress force, and energy dissipation bar diameter were kept identical. The influence of the activation displacement ratio of the energy dissipater on the hysteretic performance was investigated through comparative analysis.

4.2. Influence of the Number of Prestressing Tendons

To investigate the influence of the number of prestressing tendons on the mechanical behavior of the post-tensioned unbonded prestressed concrete beam–column joints with two-stage energy dissipation, low-cycle reversed loading analyses were performed on Case 2, Case 1, and Case 3. The results are shown in Figure 7. All three groups of joints exhibited typical flag-shaped hysteretic characteristics with full hysteretic loops, reflecting

good self-centering capacity and energy dissipation capacity. From the hysteretic curves, it can be observed that the first stiffness of the three groups remained essentially identical, indicating that variations in the number of prestressing tendons had no significant effect on the elastic-stage stiffness of the joints. This stage of stiffness was primarily governed by the beam and column members themselves and the initial contact conditions. However, the second stiffness showed a significant increasing trend. Taking the second stiffness value of Case 1 as the baseline, the second stiffness of Case 2 decreased by approximately 18.2%, while that of Case 3 increased by about 21.5%. This pattern is in full agreement with the theoretical analysis results of Huang et al. [32], namely that the second stiffness is dominated by the axial stiffness of the prestressing tendons. An increase in the number of the prestressing tendons directly enhances their axial stiffness, thereby linearly increasing the second stiffness of the joint.

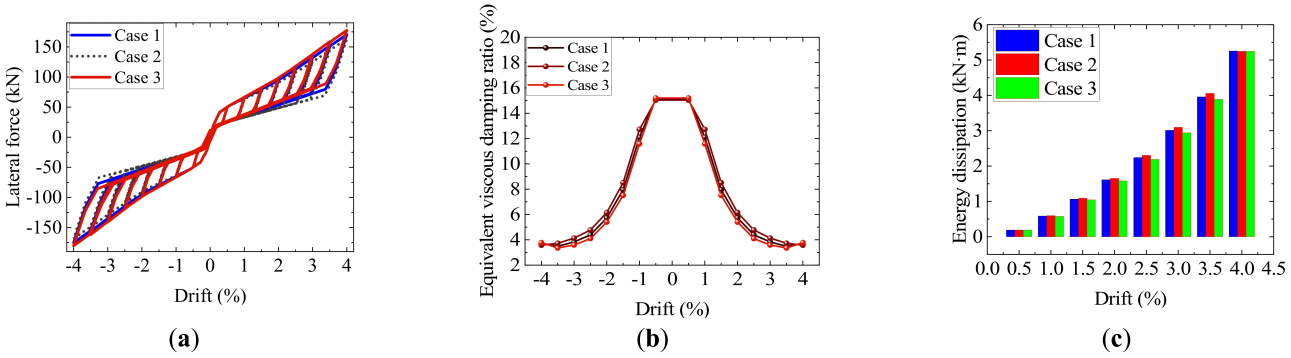


Figure 7. Performance comparison of joint with different number of the PT tendons. (**a**) Hysteresis curves. (**b**) Equivalent viscous damping coefficient. (**c**) Energy dissipation per cycle.

From the energy dissipation per cycle curves, it can be seen that the energy dissipation per cycle of the three groups increased approximately linearly with the drift ratio. At the same drift, the energy dissipation values of the three groups basically coincided. Compared with Case 1, the differences in energy dissipation per cycle for Case 2 and Case 3 were both controlled within 3%, indicating that the number of prestressing tendons had no obvious influence on the energy dissipation capacity of the joints. The energy dissipation of the joints was mainly determined by the bolt pretensioning force in the energy dissipater and the sliding distance of the friction plates, and was independent of the prestressing tendon parameters.

The equivalent viscous damping ratio curves show that the equivalent viscous damping ratios of the three groups gradually decreased and then stabilized with increasing drift ratio. At the same drift, the equivalent viscous damping ratio decreased as the number of prestressing tendons increased. Compared with Case 1, the equivalent viscous damping ratio of Case 2 increased by an average of about 7.8%, while that of Case 3 decreased by an average of about 8.3%. This is because the equivalent viscous damping ratio is the ratio of energy dissipation to total deformation energy. Under the premise that the energy dissipation capacity remained essentially unchanged, an increase in the number of prestressing tendons enhanced the flexural bearing capacity of the joint and increased the deformation energy, thereby reducing the equivalent viscous damping ratio. This reflects the synergistic regulation effect of prestressing tendons on the joint's stiffness and damping.

In summary, the number of prestressing tendons is a key parameter for regulating the stiffness and bearing capacity of post-tensioned unbonded prestressed concrete beam–column joints with two-stage energy dissipation, with no significant effect on the energy dissipation capacity. These findings provide a direct basis for the parametric optimization design of self-centering joints. By adjusting the number of prestressing tendons, a balanced

configuration can be achieved among stiffness and bearing capacity, and damping and energy dissipation.

4.3. Influence of Initial Prestress Force

To investigate the influence of initial prestress force on the hysteretic performance of the post-tensioned unbonded prestressed concrete beam–column joints with two-stage energy dissipation, low-cycle reversed loading analyses were performed on three joint groups, namely Case 4, Case 1, and Case 5. The number of prestressing tendons, bolt pretensioning force, and geometric parameters of the energy dissipater were kept unchanged, while initial prestress forces of 160 kN, 80 kN, and 300 kN were applied to the three groups, respectively. The comparative analysis results are shown in Figure 8.

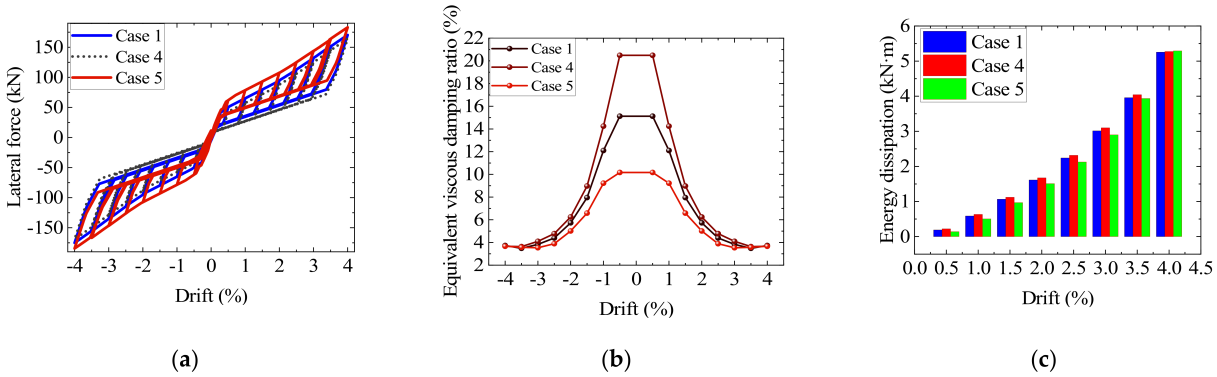


Figure 8. Performance comparison of joint with different initial PT forces. (**a**) Hysteresis curves. (**b**) Equivalent viscous damping coefficient. (**c**) Energy dissipation per cycle.

The results indicate that all three groups of joints exhibited typical flag-shaped hysteretic characteristics, demonstrating good self-centering capacity within the prestress range of 80 to 300 kN. Notably, the low-prestress joint Case 4 also maintained a complete flag-shaped hysteresis, which verifies the feasibility of the low-prestress self-centering design concept. This concept suggests that, under the premise of ensuring self-centering capacity, moderately reducing the prestress can enhance the energy dissipation ratio and maximize the energy dissipation capacity.

The joint stiffness evolution analysis shows that the first and second stiffnesses of the three groups were basically consistent. The stiffness differences between Case 4 and Case 5 were controlled within −2% to 2%. This indicates that the initial prestress force has limited influence on the stiffness at the elastic and joint-opening stages. Meanwhile, the third-stiffness mechanism ensures that the joint still possesses stiffness reserves under larger deformation, which helps achieve the design objective of efficient energy dissipation.

Further analysis of the hysteretic curves reveals that the activation force of the joints increased with the initial prestress force. This finding is consistent with the theoretical model, which states that the activation force is jointly determined by the initial tension of the prestressing tendons and the bolt pretensioning force. It thus indicates that the initial prestress force is a key parameter for regulating the activation force and self-centering capacity.

The energy dissipation per cycle analysis shows that the energy dissipation of the three groups increased steadily with the drift, and the values were highly consistent at the same drift ratio. The differences between Case 4 and Case 5 were both within 4%. This suggests that the energy dissipation capacity is mainly determined by the bolt pretensioning force and the sliding distance, while the influence of prestress on absolute energy dissipation is limited. These findings provide a theoretical basis for enhancing the energy dissipation ratio through low-prestress configuration.

The equivalent viscous damping ratio decreased and then stabilized with increasing drift ratio. At the same drift, the equivalent viscous damping ratio of the low-prestress joint was significantly higher than that of the high-prestress joint. For instance, compared with Case 1, the equivalent viscous damping ratio of Case 4 increased by an average of about 32%, while that of Case 5 decreased by an average of about 25%. This demonstrates that low prestress can significantly improve energy dissipation efficiency without sacrificing energy dissipation capacity. In contrast, high prestress configuration can enhance the flexural bearing capacity of the joint.

In summary, the initial prestress force is a key factor in regulating the joint's activation force, energy dissipation efficiency, and stiffness reserves. Its influence on the joint stiffness and absolute energy dissipation capacity is limited. Through rational design of low prestress, the synergistic optimization of energy dissipation capacity and energy dissipation efficiency can be achieved while maintaining self-centering capacity and stiffness reserves. This verifies the scientific validity of the design concept that combines low-prestress self-centering with two-stage stiffness, and provides a theoretical basis for the seismic performance design of self-centering joints.

4.4. Influence of Bolt Pretensioning Force

To investigate the influence of bolt pretensioning force on the mechanical behavior of the post-tensioned unbonded prestressed concrete beam–column joints with two-stage energy dissipation, low-cycle reversed loading numerical analyses were conducted on Case 1, Case 6, and Case 7, while keeping the number of prestressing tendons, initial prestress force, and energy dissipater parameters constant. The results are shown in Figure 9.

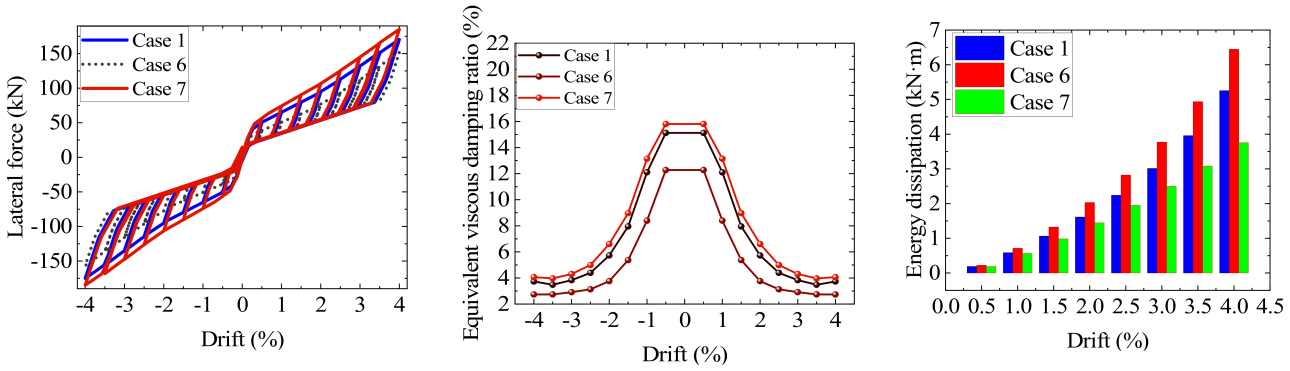


Figure 9. Performance comparison of joint with different friction forces. (**a**) Hysteresis curves. (**b**) Equivalent viscous damping coefficient. (**c**) Energy dissipation per cycle.

From the perspective of stiffness evolution characteristics, the first stiffness, second stiffness, and third stiffness of the three cases were basically consistent. Compared with Case 1, the stiffness differences at various stages for Case 6 and Case 7 were both controlled within 1.5%. This indicates that changes in bolt pretensioning force have almost no effect on the joint stiffness. The three-stage stiffness characteristics of the joint are mainly dominated by the axial stiffness of the prestressing tendons and the structural stiffness of the beam and column, and are independent of the bolt pretensioning force parameter. This feature enables the decoupled design and synergistic operation of the stiffness system and the energy dissipation system.

The bolt pretensioning force has a significant effect on the activation force of the joint. As the bolt pretensioning force increases, the activation force of the joint shows a linear increasing trend. Compared with Case 1, the activation force of Case 6 decreases

by approximately 27.6%, while that of Case 7 increases by about 35.1%. This variation pattern is in full agreement with the conclusion from the study by Huang et al. [14] that the activation force is positively correlated with the bolt pretensioning force, which confirms the reliability of the numerical simulation. The initial resistance that needs to be overcome for joint opening is composed of the contribution from prestress and the contribution from bolt pretensioning force, which directly governs the friction force. As the main variable parameter, the bolt pretensioning force directly regulates the activation force threshold.

From the energy dissipation per cycle curves in Figure 9c, it can be seen that the dissipated energy of the three groups increased linearly with the drift, and at the same drift, the dissipated energy increased significantly with the bolt pretensioning force. Compared with Case 1, the energy dissipation per cycle of Case 6 decreased by an average of about 18.2%, while that of Case 7 increased by an average of about 21.7%. This indicates that increasing the bolt pretensioning force is a direct and effective means to enhance the energy dissipation capacity and improve the energy dissipation ratio of the joint. Combined with the low-prestress configuration concept proposed in this study, on the premise of ensuring self-centering capacity, appropriately increasing the bolt pretensioning force can significantly enhance the absolute energy dissipation capacity of the joint without altering the stiffness characteristics.

The comparison of equivalent viscous damping ratios is shown in Figure 9b. For all three cases, the equivalent viscous damping ratio gradually stabilized with increasing drift, and at the same drift, the damping ratio increased synchronously with the bolt pretensioning force. Compared with Case 1, the damping ratio of Case 6 decreased by an average of about 15.4%, while that of Case 7 increased by an average of about 17.9%. The underlying mechanism for this pattern is that the equivalent viscous damping ratio is the ratio of energy dissipation to total deformation energy. An increase in bolt pretensioning force directly enhances the energy dissipation capacity, while the change in joint bearing capacity is relatively small, thereby leading to a significant increase in the damping ratio.

Overall, compared with Case 1, Case 7 exhibits an approximately 21.7% increase in energy dissipation capacity and a 17.9% rise in equivalent viscous damping ratio. Concurrently, the tertiary stiffness mechanism provides a stiffness guarantee for configurations with high bolt pretensioning forces under strong seismic events. As the displacement enters the third stage, the third stiffness K_3 generated by the bearing action of the energy dissipation bars becomes active, ensuring that the structure maintains adequate lateral stiffness. This establishes a synergistic working mode in which the friction system regulates both energy dissipation and activation force while the third stiffness ensures safety under severe seismic conditions.

It is worth noting that the regulating effect of bolt pretensioning force and that of prestress are independent and do not interfere with each other. A low-prestress configuration increases the energy dissipation ratio, while a high bolt pretensioning force configuration directly enhances the energy dissipation capacity. These two parameters can therefore be combined for optimization. By adopting a low prestress level together with an appropriately high bolt pretensioning force, greater absolute energy dissipation capacity can be achieved while maintaining a high energy dissipation ratio, and the tertiary stiffness mechanism mainly guarantees safety. This parameter decoupling characteristic provides considerable design flexibility for performance optimization of post-tensioned unbonded prestressed concrete beam–column joints.

In conclusion, bolt pretensioning force serves as a core parameter for regulating the activation force threshold and energy dissipation performance of post-tensioned unbonded prestressed concrete beam–column joints with two-stage energy dissipation, while having no significant effect on joint stiffness. Through reasonable configuration of a higher bolt

pretensioning force, the energy dissipation capacity and energy dissipation efficiency of the joint can be effectively improved without compromising self-centering capacity or stiffness reserves. This provides solid theoretical and data support for the optimization design of such joints.

4.5. Influence of Diameter Energy Dissipation Bar

To investigate the influence of energy dissipation bars on the mechanical behavior of the post-tensioned unbonded prestressed concrete beam–column joints with two-stage energy dissipation, low-cycle reversed loading analyses were conducted on Case 1, Case 8, and Case 9, while keeping the other parameters constant. The results are shown in Figure 10. Compared with Case 1, the diameters of energy dissipation bars in Case 8 and Case 9 were increased by approximately 20% and 40%, respectively. All three groups of joints exhibited full and stable flag-shaped hysteretic characteristics, indicating that good self-centering capacity was maintained under different energy dissipation bar configurations.

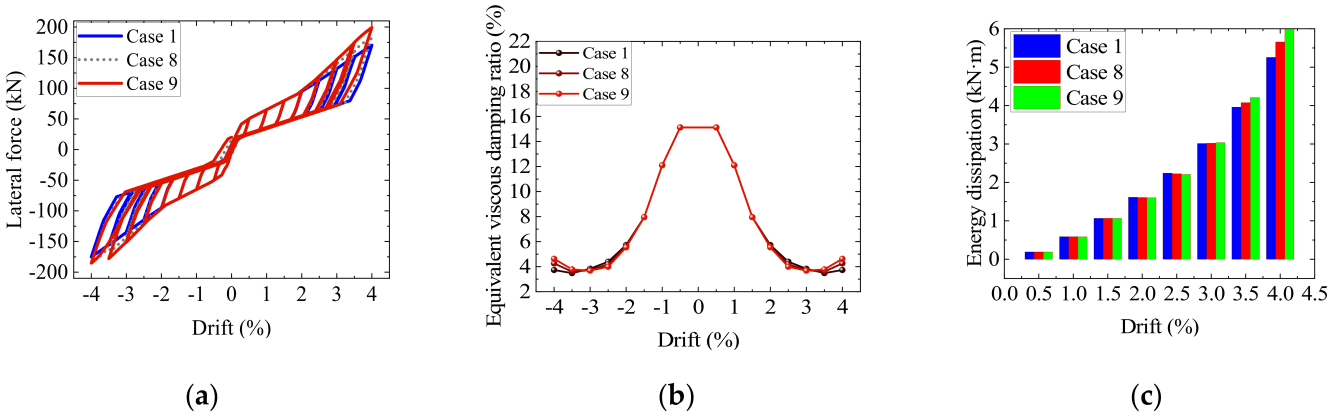


Figure 10. Performance comparison of joint with energy dissipation bars. (**a**) Hysteresis curves. (**b**) Equivalent viscous damping coefficient. (**c**) Energy dissipation per cycle.

From the perspective of stiffness evolution, the first and second stiffnesses were basically unaffected by the diameter of energy dissipation bar. Compared with Case 1, the differences in the first and second stiffnesses of Case 8 and Case 9 were both controlled within 1.5%. However, the third stiffness showed significant differences. The third stiffness of Case 8 was about 110% higher than that of Case 1, and that of Case 9 was about 230% higher. This pattern is consistent with theoretical expectations. The third stiffness is dominated by the compression-bearing mechanism of the energy dissipation bars, and its value is independent of the prestressing system and the friction system, allowing direct control of the stiffness reserve.

From the energy dissipation per cycle curves in Figure 10c, it can be seen that at the small drift stage, within 2%, the dissipated energy of the three groups basically coincided, with differences within 1.5%. This suggests that the parameters of energy dissipation bar have no obvious influence on the energy dissipation capacity of the joint under minor deformation. As the drift increased and entered the third stage, the energy dissipation differences gradually emerged. At a drift of 4%, compared with Case 1, the energy dissipation per cycle of Case 8 increased by about 8.3%, and that of Case 9 increased by about 14.6%. The reason is that the increase in third stiffness causes the joint to withstand higher loads at the ultimate displacement, and the energy dissipated by the bending deformation of the energy dissipation bars increases accordingly, thereby slightly improving the total energy dissipation capacity.

The equivalent viscous damping ratio responses are shown in Figure 10b. For all three groups, the damping ratio first increased and then stabilized with increasing drift. At the small drift, the curves basically coincided. After entering the third stage, the damping ratio slightly increased with the energy dissipation bar diameter. At a drift ratio of 4%, compared with Case 1, the equivalent viscous damping ratio of Case 8 increased by about 4.2%, and that of Case 9 increased by about 7.1%. This indicates that increasing the energy dissipation bar diameter can slightly improve the energy dissipation efficiency of the joint at large displacements, but its main contribution remains providing stiffness rather than energy dissipation.

The core role of the energy dissipation bars is concentrated on the stiffness guarantee under larger deformation. From the hysteretic curves in Figure 10a, it can be observed that when the drift ratio exceeded 3%, the slopes of the hysteretic curves for Case 8 and Case 9 increased significantly, and the rate of bearing capacity increase was much higher than that of Case 1. At a drift of 4%, compared with Case 1, the peak load of Case 8 increased by about 15.3%, and that of Case 9 increased by about 28.7%. This means that under larger deformation, joints with larger energy dissipation bar diameters can provide greater lateral stiffness and bearing capacity reserves for the structure, thereby effectively controlling deformation and preventing collapse.

The regulating effect of the energy dissipation bars is independent of those of the prestress and the bolt pretensioning force. Combined with the design concept of this paper, the low-prestress configuration ensures self-centering capacity and a high energy dissipation ratio, the bolt pretensioning force regulates the overall energy dissipation level, and the energy dissipation bar parameters predominantly control the stiffness reserve under larger deformation. The three together form a multi-dimensional synergistic regulation system. Low prestress optimizes the energy dissipation efficiency, bolt pretensioning force guarantees the total energy dissipation, and energy dissipation bars ensure safety.

In general, while maintaining the same self-centering capacity and energy dissipation level as Case 1, Case 9 achieved a peak bearing capacity that was about 28.7% higher and an energy dissipation capacity that was about 14.6% higher. This indicates that the parameters of energy dissipation bar are key to ensuring the safety of the joint, and their values can be designed according to the deformation control requirements of the structure.

In summary, the third stiffness is the core parameter for regulating the stiffness reserve and ultimate bearing capacity of the joint under larger deformation, and it has no significant effect on the first and second stiffnesses or the energy dissipation capacity. By setting a higher third stiffness through changes in the material and diameter of the energy dissipation bars, the safety reserves of the joint under can be significantly enhanced while maintaining the advantages of low-prestress self-centering and the friction energy dissipation capacity. This achieves the collaborative optimization design objective of improving efficiency through low prestress, guaranteeing the energy dissipation amount through friction dissipation, and ensuring safety through third stiffness.

4.6. Influence of Activation Displacement Ratio

To investigate the influence of the secondary activation behavior of the energy dissipater on the mechanical behavior of the joint, low-cycle reversed loading analyses were conducted on three joint groups, namely Case 1, Case 10, and Case 11, while keeping parameters such as the number of steel strands, initial prestress force, energy dissipation bar diameter, and bolt pretensioning force constant. The results are shown in Figure 11.

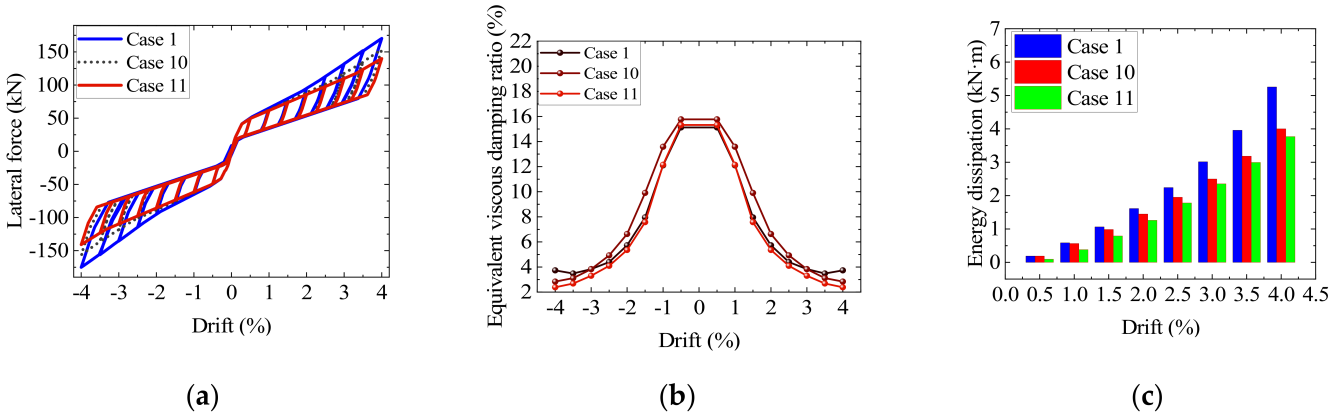


Figure 11. Performance comparison of joint with different activation displacement ratio. (**a**) Hysteresis curves. (**b**) Equivalent viscous damping coefficient. (**c**) Energy dissipation per cycle.

From the hysteretic curves, it can be observed that the first and second stiffnesses of the three groups were basically consistent. However, significant differences existed in the activation displacement of the third stiffness. This is because the activation displacement ratio is directly determined by the pure friction sliding segment. As the length of the pure friction segment increases, the drift ratio corresponding to the activation of the third stiffness is gradually delayed. Compared with Case 10, the activation drift of the third stiffness in Case 1 increased by approximately 18.3%, and that in Case 11 was delayed by about 22.6%. This pattern is consistent with theoretical expectations. The length of the friction segment directly determines the threshold at which the energy dissipation bars in the energy dissipater contact the hole wall and enter the second stage. It is a key parameter for regulating the activation timing of the third stiffness.

As the length of the pure friction segment in the first stage of the energy dissipater increases, the energy dissipation per cycle of the joint changes significantly. Compared with Case 1, the energy dissipation per cycle of Case 10 decreased by an average of about 22.3%, and that of Case 11 decreased by an average of about 34.7%. This indicates that an excessively long friction segment length weakens the energy dissipation efficiency of the joint, while moderately reducing the friction segment length is more conducive to improving the energy dissipation capacity per unit displacement. This is consistent with the design concept of this paper, which optimizes the energy dissipation ratio through a low-prestress configuration.

Figure 11b compares the equivalent viscous damping ratio responses. For all three groups, the equivalent viscous damping ratio gradually stabilized with increasing drift ratio. At the same drift ratio, the equivalent viscous damping ratio decreased as the friction segment length increased. Compared with Case 1, the equivalent viscous damping ratio of Case 10 decreased by an average of about 16.8%, and that of Case 11 decreased by an average of about 29.5%. This pattern intuitively reflects the regulating effect of the friction segment length on the energy dissipation efficiency. Based on the low prestress that ensures self-centering performance, a shorter friction segment length allows the energy dissipater to enter the high-efficiency sliding energy dissipation stage earlier, thereby increasing the equivalent viscous damping ratio and the energy dissipation ratio. Conversely, a longer friction segment length delays the activation of energy dissipation and reduces the energy dissipation efficiency per unit deformation.

Meanwhile, the third stiffness and activation force of the three groups were basically consistent, indicating that the friction segment length only regulates the energy dissipation process and does not affect the stiffness reserve or bearing capacity threshold of the joint.

In summary, the length of the pure friction segment in the first stage of the energy dissipater is a key parameter for regulating the activation timing of the third stiffness and the stage distribution of the energy dissipation mechanism. It has no significant effect on the first and second stiffnesses. Through reasonable configuration of the friction segment length, the stiffness and energy dissipation distribution of the joint at different deformation stages can be optimized while maintaining self-centering capacity and the overall energy dissipation level, further enhancing the adjustability of the seismic performance of the beam–column joint.

It should be noted that all parameter combinations were screened for tendon yielding/rupture, concrete crushing, local bearing, ED bar fracture, bolt slip/preload loss, plate yielding/buckling, and reinforcement strain limits. The ranges adopted fall within these limits. However, the results are presented as parametric observations rather than design-ready recommendations.

5. Discussion

Table 3 presents the quantitative comparison with previously known similar studies. The parametric results obtained in this study provide a quantitative basis for comparing the seismic behavior of the proposed two-stage energy dissipation joint with that of previously investigated self-centering connections. Conventional post-tensioned unbonded prestressed concrete joints predominantly rely on a single friction-based or yielding-type energy dissipation mechanism [9–11,17,18], which leads to an abrupt stiffness degradation after joint opening and couples the energy dissipation capacity with the prestress level. This composite "friction–bending" mechanism represents a fundamental departure from earlier single-mechanism designs and aligns with, yet extends, the preliminary experimental validation reported by Huang et al. [22], which was limited to three design variables. By expanding the parameter space to five independent variables and eleven analysis cases, the present study establishes quantitative influence laws that were previously unavailable.

Table 3. Quantitative comparison with previously known similar studies.

Aspect	Existing Studies	Present Findings	Difference
Dissipation mechanism	Single friction or yielding [12–14]	Two-stage friction–bending composite dissipation	First implementation of secondary activation with a stable third stiffness K_3 in a concrete joint
Low-prestress effect	Low prestress applied only to steel braces [30,31]	Low prestress increases equivalent viscous damping by ~32%	Quantifies the damping enhancement for concrete frames
Parameter decoupling	Prestress and dissipation coupled [27,28]	Friction force linearly governs activation without affecting stiffness; third stiffness mainly controlled by ED bars	First clear statement of a three-path decoupled design framework

A key scientific insight developed here is the explicit decoupling of three design pathways: (1) number of prestressing tendons governs the second stiffness and bearing capacity without affecting the energy dissipation per cycle; (2) the initial prestress force regulates the equivalent viscous damping ratio, while having limited influence on absolute energy dissipation or stiffness; and (3) the bolt pretensioning force is linearly and positively correlated with the activation force and can enhance the energy dissipation per cycle by up to 21.7% without altering any stage stiffness. These findings provide a theoretical framework for low-prestress self-centering design that maximizes the energy dissipation ratio β while maintaining re-centering capability and stiffness reserves. Furthermore, the

third stiffness K_3, dominated entirely by the compression-bearing action of the ED bars, offers an independent safety guarantee: increasing the ED bar diameter raises the peak loading capacity by 28.7% at a 4% drift, a feature absent in conventional flag-shaped hysteretic systems.

Based on the hysteretic behavior established in this study, the prospects for implementing the proposed post-tensioned unbonded prestressed concrete beam–column joint in real-world projects can be clearly stated. Owing to its flag-shaped self-centering characteristic combined with a two-stage energy dissipation mechanism, the joint is particularly well-suited for the following types of construction projects. First, in precast concrete frame structures located in high-seismic regions (e.g., schools, hospitals, and other critical public facilities), the joint provides stable energy dissipation while the low-prestress strategy minimizes post-earthquake residual deformation, facilitating rapid functional recovery. Second, for structures with stringent residual drift limits (e.g., urban viaduct pier–beam joints, data centers), the third stiffness K_3 offers additional lateral stiffness and a bearing capacity reserve (28.7% higher at 4% drift), while the linear friction dissipation behavior ensures that energy dissipaters do not require replacement after an event. Finally, the three-parameter design pathway enables performance-based seismic design: designers can adjust the prestress level, bolt pretension, and ED bar diameter to meet distinct seismic defense objectives, thereby providing a quantifiable and customizable engineering solution for enhancing the seismic resilience of precast concrete structures.

6. Conclusions

6.1. Scientific Results

This study conducted refined finite element simulations and parametric analyses on a novel post-tensioned unbonded prestressed concrete beam–column joints with two-stage energy dissipation, and clarified the influence mechanisms of core design parameters on its hysteretic performance. The main research conclusions are as follows.

(1) The joint breaks through the limitation of the single energy dissipation mode in traditional post-tensioned unbonded prestressed concrete joints by adopting a two-stage energy dissipation mechanism of friction slip and bending compression-bearing. Under the premise of ensuring post-earthquake self-centering capacity, the low-prestress strategy significantly improves the energy dissipation ratio. The secondary activation of the energy dissipation bars forms a stable third stiffness, which effectively suppresses stiffness degradation under larger deformation. The hysteretic curves are full and exhibit a typical flag shape, combining excellent energy dissipation potential with deformation control capability.

(2) The number of the prestressing tendons only changes the second stiffness and flexural bearing capacity of the joint, and has no obvious effect on the energy dissipation capacity. Increasing or decreasing the number of prestressing tendons by 25% causes a corresponding change of about 20% in the second stiffness, but the difference in energy dissipation per cycle is controlled within 3%. Flexible matching of stiffness and bearing capacity can be achieved by adjusting the number of the prestressing tendons.

(3) The initial prestress force has a weak influence on the joint stiffness and absolute energy dissipation, but its regulating effect on the equivalent viscous damping ratio is significant. Reducing the initial prestress force can increase the equivalent viscous damping ratio by an average of about 32%. This verifies the advantage of the low-prestress design in improving energy dissipation efficiency.

(4) The bolt pretensioning force is a core parameter for regulating the activation force and energy dissipation capacity. It is linearly and positively correlated with the activation force, and has no effect on the stiffness at each stage of the joint. Increasing the bolt

pretensioning force by about 30% can increase the energy dissipation per cycle by an average of 21.7% and the equivalent viscous damping ratio by 17.9%, thus realizing the decoupled design of the energy dissipation system and the stiffness system.

(5) The third stiffness is predominantly controlled by the compression-bearing mechanism of the energy dissipation bars. The energy dissipation bar parameters have almost no effect on the first and second stiffnesses. After increasing the third stiffness by 2.1 times, the peak bearing capacity of the joint at a drift ratio of 4% is improved by 28.7%, and the energy dissipation per cycle is slightly increased by 14.6%. This provides an independent regulation path for the design of stiffness reserves.

(6) The activation displacement ratio is a key parameter controlling the hysteretic shape. As the activation displacement ratio increases from 0.25 to 0.50, the pure-friction stage becomes longer and the second-stage activation is delayed. Conversely, a smaller activation displacement ratio causes earlier engagement of the ED bars and a steeper transition into the third stage. This result is directly supported by the numerical parametric study.

The parameter recommendations in this study are based on component-level numerical simulations and have not been validated through system-level design checks or full-scale dynamic tests. They should not be used as standalone design guidelines without further evaluation of the above failure modes under realistic loading conditions.

6.2. Applied Results

Based on the established hysteretic behavior, the proposed joint is most effective in three types of construction projects. Precast concrete frames in high seismic regions, such as schools and hospitals, can benefit from the stable energy dissipation under strong earthquakes and the minimized residual deformation enabled by the low prestress strategy, which facilitates rapid post-earthquake functional recovery. Structures with stringent residual drift limits, including urban viaduct pier beam joints and data centers, are well suited to the flag shaped self-centering characteristic and the third stiffness K_3, which provides an additional bearing capacity reserve of 28.7% at 4% drift to prevent collapse. Mid-rise buildings requiring performance-based customization can take advantage of the decoupled three parameter design, where prestress level, bolt pretension, and energy dissipation bar diameter are adjusted to meet distinct seismic defense objectives, thereby offering a quantifiable and customizable engineering pathway for enhancing the seismic resilience of precast concrete structures.

6.3. Future Research Prospects

The present study is limited to short-term quasi-static cyclic behavior. In long-term service, the self-centering capability and activation forces may be affected by prestress relaxation, anchorage seating loss, concrete creep and shrinkage, bolt-preload loss, friction-surface wear, and variation in the friction coefficient. These time-dependent and cyclic wear effects are not captured by the current model. Future work should include (i) accelerated aging tests to quantify prestress loss and anchorage seating under sustained load, (ii) cyclic slip-compression tests to evaluate friction-surface wear and the evolution of the friction coefficient, and (iii) long-term monitoring of full-scale specimens to validate the durability of the two-stage energy dissipation system.

Author Contributions: Conceptualization, Q.Z. and L.H.; Methodology, Q.Z. and L.H.; Software, Y.Z.; Validation, Q.Z.; Formal analysis, L.H.; Investigation, Y.Z.; Data curation, L.H.; Writing—original draft, Q.Z., X.S., L.H. and Y.Z.; Writing—review & editing, X.S.; Visualization, X.S. and L.H.; Supervision, Y.Z.; Funding acquisition, X.S. All authors have read and agreed to the published version of the manuscript.

Funding: The research described in this paper was sponsored by the Jiangsu Province Qinglan Project Funded Project.

Data Availability Statement: The data presented in this study are available on request from the corresponding author. The data are not publicly available due to they form part of an ongoing research project.

Conflicts of Interest: The authors declare no conflicts of interest.

References

1. Lin, Y.; Fu, Y.; Sun, J.; Li, H.; Zhang, K.; Wang, L. Robust seismic response evaluation considering an uncertainty emerging in asymmetric bridges. *Reliab. Eng. Syst. Saf.* **2025**, *266*, 111740. [CrossRef]
2. Zhang, Y.; Xia, B.; Guo, X.; Sun, B.; Hu, D.; Wei, Y. Genetic algorithm-enhanced Housner intensity measure for seismic vulnerability analysis of reinforced concrete column-steel beam (RCS) frame structure. *Soil Dyn. Earthq. Eng.* **2025**, *193*, 109320. [CrossRef]
3. Hou, F.; Chong, W.; Lin, Y.; Li, M.; Wang, Q.; Chen, Z. Modified energy-based design method of the precast partially steel-reinforced concrete beam–CFST column eccentrically braced frame. *Buildings* **2025**, *15*, 1797. [CrossRef]
4. Wen, J.Y.; Zhou, H.Y.; Li, X.X.; Zhang, Y.T. A rapid identification framework for post-earthquake local damage of the multi-span interconnected slender equipment in substation. *Eng. Struct.* **2025**, *333*, 120124. [CrossRef]
5. Sun, G.; Wang, Y.; Liu, W.; Zhang, H.; Chen, J.; Li, X. Experimental investigation of self-centering beam-to-column connections with different ribbed top and seat angles. *Structures* **2024**, *60*, 105859. [CrossRef]
6. Wu, Z. Seismic performance of full-scale self-centering reinforced concrete beam-column joints: Experimental, numerical and theoretical analysis. *J. Build. Eng.* **2023**, *78*, 107683. [CrossRef]
7. Di, J.; Zhou, X.; Han, B.; Liu, Y.; Wang, C.; Zhang, L. Experimental study on hysteretic performance of self-centering energy dissipation beam-to-column connections equipped with SMA plates. *J. Build. Eng.* **2024**, *82*, 108321. [CrossRef]
8. Huang, W.; Hu, G.X.; Miao, X.W.; Li, Y.; Zhang, P.; Chen, S. Seismic performance analysis of a novel demountable precast concrete beam-column connection with multi-slit devices. *J. Build. Eng.* **2021**, *44*, 102663. [CrossRef]
9. Hu, Q.; Qin, J.; Zhang, W.; Zhang, M. Theoretical analysis model of a new post-tensioned, unbonded, prestressed beam–column connection. *Buildings* **2025**, *15*, 2823. [CrossRef]
10. Zhong, Q.; Tao, Z.; Cao, W.; Dong, Q. Experimental study and theoretical analysis on seismic performance of post-tensioned hybrid beam–column connection with replaceable energy dissipation devices. *Structures* **2026**, *86*, 111380. [CrossRef]
11. Yu, J.; Yan, X.; Wang, G.; Chen, W.; Shi, S.; Lin, Z. Hysteretic behavior of prefabricated self-centering RC beam–CFDST column joints. *Structures* **2025**, *80*, 110007. [CrossRef]
12. Morgen, B.G.; Kurama, Y.C. Seismic response evaluation of posttensioned precast concrete frames with friction dampers. *J. Struct. Eng.* **2008**, *134*, 132–145. [CrossRef]
13. Cheng, S.; Guo, T.; Xie, T.; Shi, X. Experimental evaluation of multi-story self-centering prestressed concrete frames with web friction devices under cyclic loading. *Eng. Struct.* **2025**, *323*, 119243. [CrossRef]
14. Huang, L.; Zhou, Z.; Wei, Y.; Xie, Q.; Sun, X. Seismic performance and resilience assessment of friction damped self-centering prestressed concrete frames. *Eng. Struct.* **2022**, *263*, 114346. [CrossRef]
15. Lu, X.; Zhang, J.; Lei, J.H. Seismic loss assessment and cost-benefit analysis of RC frames with self-centering friction joints. *Eng. Struct.* **2026**, *351*, 122085. [CrossRef]
16. Qiu, C.X.; Liu, J.W.; Du, X.L. Cyclic behavior of SMA friction damper. *Eng. Struct.* **2022**, *250*, 113407. [CrossRef]
17. Koshikawa, T. Moment and energy dissipation capacities of post-tensioned precast concrete connections employing a friction device. *Eng. Struct.* **2017**, *138*, 170–180. [CrossRef]
18. Kammula, V.; Erochko, J.; Kwon, O.S.; Christopoulos, C. Application of hybrid-simulation to fragility assessment of the telescoping self-centering energy dissipative bracing system. *Earthq. Eng. Struct. Dyn.* **2014**, *43*, 811–830. [CrossRef]
19. Wu, H.; Zhou, Y.; Liu, W. Collapse fragility analysis of self-centering precast concrete walls with different post-tensioning and energy dissipation designs. *Bull. Earthq. Eng.* **2019**, *17*, 3593–3613. [CrossRef]
20. Zhao, Z.; Xu, L.; Lyu, Y. Seismic performance of an innovative precast RC beam–column joint incorporating self-centering rebar couplers: Experimental investigation. *J. Build. Eng.* **2025**, *115*, 114556. [CrossRef]
21. Li, Y.; Wang, Z.; Pang, R.; Zhou, C. Parametric study on self-centering precast concrete frame connections with integrated composite damping. *J. Earthq. Eng.* **2025**, *30*, 1587–1612. [CrossRef]
22. Wang, S.; Zhou, X.; Yuan, G.; Zhang, D.; Huang, L.; Wei, Y. Seismic performance and architectural function recoverability for self-centering precast concrete frames with enhanced post-stiffness and energy dissipation. *Buildings* **2025**, *15*, 3949. [CrossRef]
23. Komvijit, T.; Chaisanit, A.; Yooprasertchai, E.; Leelataviwat, S. Experimental and numerical study of precast concrete joints with buckling-restrained knee braces and self-centering tendons. *Structures* **2025**, *82*, 110524. [CrossRef]

24. Wang, S.; Zhang, T.; Xu, W.; Du, D.; Zhang, Y. Experimental and numerical investigations on novel post-tensioned precast beam-to-column energy-dissipating connections. *Structures* **2023**, *54*, 117–133. [CrossRef]
25. Yılmaz, O.; Oğuz, L. Numerical investigation of RC beams with an integrated frictional and elastomeric seismic device. *Period. Polytech. Civ. Eng.* **2026**, *70*, 698–716. [CrossRef]
26. Guo, T.; Zhu, R.; Lu, S.; Chai, S. Long-term behavior of the self-centering post-tensioned concrete frame with web friction devices: Experimental and numerical models. *J. Build. Eng.* **2025**, *111*, 117152. [CrossRef]
27. El-Sheikh, M.; Sause, R.; Pessiki, S.; Lu, L.W. *Seismic Analysis, Behavior, and Design of Unbonded Post-Tensioned Precast Moment Frames (Report No. EQ-97-02)*; Department of Civil and Environmental Engineering, Lehigh University: Bethlehem, PA, USA, 1997.
28. Stone, W.; Cheok, G.; Stanton, J. Performance of hybrid moment-resisting precast beam-column concrete connections subjected to cyclic loading. *ACI Struct. J.* **1995**, *92*, 229–249. [CrossRef] [PubMed]
29. Huang, L.; Shi, Z.; Zeng, B.; Tian, H. Self-centering prestressed concrete frames with low prestressing and slope friction: Design method and seismic performance. *Bull. Earthq. Eng.* **2026**, *24*, 2069–2105. [CrossRef]
30. Xiao, Y.; Eberhard, M.O.; Zhou, Y.; Li, H. Experimental investigation of a low-prestressed self-centering energy dissipative brace. *Earthq. Eng. Struct. Dyn.* **2022**, *51*, 1457–1476. [CrossRef]
31. Zheng, J.; Zhou, Z.; Zeng, B.; Huang, L. Seismic resilience analysis of self-centering prestressed concrete frames with generalized flag-shaped hysteretic behavior. *Eng. Struct.* **2023**, *297*, 116947. [CrossRef]
32. Huang, L.; Zhu, Y.; Xu, Q.; Zeng, B.; Tian, H. Experimental study and theoretical analysis of self-centering concrete beam-column connections characterized by friction-bending energy dissipation and low-prestressing. *J. Build. Eng.* **2026**, *123*, 115890. [CrossRef]
33. Sucuoglu, H. Effect of connection rigidity on seismic response of precast concrete frames. *PCI J.* **1995**, *40*, 94–103. [CrossRef]
34. Imoh, U.U.; Habashneh, M.; Hassan, R.; Kaine, S.C.; Babafemi, A.J.; Movahedi-Rad, M. Metakaolin-enhanced laterite rock aggregate concrete: Strength optimization and sustainable cement replacement. *Buildings* **2025**, *15*, 4553. [CrossRef]
35. Imoh, U.U.; Apata, A.C.; Movahedi-Rad, M. Performance of concrete incorporating waste glass cullet and snail shell powder: Workability and strength characteristics. *Buildings* **2025**, *15*, 2161. [CrossRef]

Disclaimer/Publisher's Note: The statements, opinions and data contained in all publications are solely those of the individual author(s) and contributor(s) and not of MDPI and/or the editor(s). MDPI and/or the editor(s) disclaim responsibility for any injury to people or property resulting from any ideas, methods, instructions or products referred to in the content.